ELSEVIER

Journal of Fluids and Structures 23 (2007) 85–100

JOURNAL OF
FLUIDS AND
STRUCTURES

www.elsevier.com/locate/jfs

Multi-resolution analysis of the large-scale coherent structure in a turbulent separation bubble affected by an unsteady wake

Sejong Chun[a], Ying Zheng Liu[b], Hyung Jin Sung[c,*]

[a]*Korea Research Institute of Standards and Science, Division of Physical Metrology, 1 Doryong-dong, Yusong-gu,*
Daejeon 305-340, Korea
[b]*Shanghai Jiao Tong University, School of Mechanical Engineering, 1954 Huashan Road, 200030, Shanghai, China*
[c]*Korea Advanced Institute of Science and Technology, Department of Mechanical Engineering, 373-1 Guseong-dong, Yuseong-gu,*
Daejeon 305-701, Korea

Received 4 November 2005; accepted 15 July 2006
Available online 22 September 2006

Abstract

Multi-resolution analysis (MRA) was applied to the large-scale coherent structure in a turbulent separation bubble affected by an unsteady wake. The unsteady wake was generated using a spoked-wheel type wake generator, which was installed in front of the separation bubble. The wake generator was rotated either clockwise (CW) or counter-clockwise (CCW) with a normalized passing frequency of $\mathrm{St}_H = 0.2$. The Reynolds number based on the half-thickness of the blunt body was $\mathrm{Re}_H = 5600$. To show the unsteady dynamic flow structures between the 'cutting' and 'wrapping' regimes, a MRA using the maximal overlap discrete wavelet transform (MODWT) was performed. This method enabled delineation of the coherent structure of the turbulent separation bubble through a scale-resolved analysis. Reconstruction of the flow field in combination with conditional averaging was attempted. Flapping motions as well as sawtooth movements of the unsteady separation bubble were analyzed using the MODWT. The unsteady wakes decayed faster in the system with CCW rotation than in that with CW rotation.

Keywords: Turbulent separation bubble; Unsteady wake; Multi-resolution analysis

---

1. Introduction

In various industrial situations, unsteady wakes influence the characteristics of a turbulent separation bubble. A striking example of this phenomenon can be found in systems containing an alternating arrangement of stationary and rotating blade rows, in which the turbulent separation bubble over one blade is periodically subjected to the unsteady wakes of upstream blades. The unsteady wake, which is characterized by a defect in the mean velocity profile and by locally intensified turbulence intensity, dramatically influences the unsteady behavior of the turbulent separation bubble. The dynamics of the unsteady flow behavior are usually related to unwanted phenomena such as energy loss, structural vibration and sound radiation. Accordingly, in-depth analysis of the processes underlying the complex interactions between a turbulent separation bubble and an unsteady wake is sorely needed.

---

[*] Corresponding author. Tel.: +82 42 869 3027; fax: +82 42 869 5027.
E-mail address: hjsung@kaist.ac.kr (H.J. Sung).

0889-9746/$ - see front matter © 2006 Elsevier Ltd. All rights reserved.
doi:10.1016/j.jfluidstructs.2006.07.002

Nomenclature

a	time scale dilation parameter (s)
b	time transition parameter (s)
D_j	wavelet detail
f	frequency (Hz)
f_m	maximum frequency by the MODWT (Hz)
f_p	wake passing frequency (Hz)
H	half-thickness of the blunt body (mm)
$\tilde{H}_f$	wavelet filter in frequency domain
j	level of wavelet filter
k	turbulent kinetic energy ($\mathrm{m}^2/\mathrm{s}^2$)
Re_d	Reynolds number based on a cylindrical rod, $U_\infty d/v$
Re_H	Reynolds number based on a blunt body, $U_\infty H/v$
S_j	wavelet smooth
St	normalized frequency, Strouhal number, fH/U_∞
St_H	normalized wake passing frequency, f_pH/U_∞
T	characteristic time scale (s)
U_∞	mainstream velocity (m/s)
u	instantaneous mainstream velocity (m/s)
wf	continuous wavelet transform coefficient
wc	wavelet auto-correlation function
x	main flow direction (mm)
x_R	reattachment length with wake generation (mm)
x_{R0}	reattachment length without wake generation (mm)
Δx	distance in the main-flow direction (mm)
y	wall normal direction (mm)

Greek symbols

v	kinematic viscosity (m/s^2)
τ	time delay parameter (s)
Ψ	Mexican hat wavelet
ω_z	spanwise vorticity (m^2/s)

Acronyms

CA	conditional averaging
CW	clockwise direction of rotation
CCW	counter-clockwise direction of rotation
CWT	continuous wavelet transform
DWT	discrete wavelet transform
MODWT	maximal overlap discrete wavelet transform

Numerous studies have investigated the influence on a separation bubble of unsteady wakes induced by the passage of upstream blade rows. Among the phenomena examined in these studies, the interaction between an unsteady wake and transition, and heat transfer of boundary layers over blade surfaces received considerable attention (Han et al., 1993; Funazaki, 1996a, b; Liu and Rodi, 1992, 1994; Minniti III and Mueller, 1998). Subsequently, Chun and Sung (2002, 2003) employed the simplified configuration of a blunt body with an upstream wake generator to study the interaction between the unsteady wakes of the wake generator and the turbulent separation bubble over the blunt body. They found that the time-mean characteristics of the separation bubble depended on the rotational direction and speed of the wake generator. In the later of the two studies, they explained the effect of unsteady wakes on the separation bubble in terms of large-scale vortical structures. More recently, Chun et al. (2004) sought to use unsteady wakes to control the turbulent separated and reattaching flow over a backward-facing step. They found that applying an unsteady wake reduced the reattachment length and suppressed the low-frequency dipole sound source. However, to-date no extensive unsteady analysis has been conducted on the interaction between unsteady wakes and a turbulent separation bubble.

As a sequel to the previous work of Chun and Sung (2002, 2003), the present study was directed toward delineating the dynamic flow structures of a turbulent separation bubble affected by unsteady wakes. In this study, large-scale turbulent structures were analyzed using multi-resolution analysis (MRA), and the flow configuration was the same as that of Chun and Sung (2002). Two wake-passing frequencies ($\mathrm{St}_H = 0$ and 0.2) were chosen for comparison. The wake generator was rotated in either a clockwise (CW) or counter-clockwise (CCW) direction, yielding entirely different flow structures (Chun and Sung, 2002). Measurements of wall-pressure and velocity fluctuations were simultaneously conducted using a microphone array and a hot-wire anemometer, respectively. The single-point wall-pressure at the corresponding reattachment point was used as a conditional signal. In conjunction with the conditional signal, MRA based on the continuous wavelet transform (CWT) and the maximal overlap discrete wavelet transform (MODWT) were used to delineate the size-variant flow structures (Li, 2002). The behavior of the turbulent separation bubble interacting with the unsteady wake was determined using the conditional averaging method (Lee and Sung, 2002; Chun and Sung, 2003, 2004; Liu et al., 2005). The scale-variant flow structures obtained using the MODWT convincingly exhibited differences between the ‘cutting’ and ‘wrapping’ regimes of the unsteady wakes (Chun and Sung, 2002, 2003). The flapping motions and sawtooth movements of the streamwise velocity near the wall were clearly disclosed.

2. Experimental apparatus

Experiments were performed in the subsonic open-circuit wind tunnel that was utilized in the previous studies by Chun and Sung (2002, 2003). Fig. 1 illustrates the front view of the flow configuration, in which 24 cylindrical rods 400 mm in length and 10 mm in diameter are attached to a wake generator. The wake generator is located upstream of a blunt body with dimensions of 350 mm (width) × 30 mm (thickness) × 550 mm (length). This configuration allows the imposition of a periodic wake flow on the turbulent separation bubble over the blunt body. The characteristic length was defined as half of the thickness of the blunt body, i.e., $H = 15\,\text{mm}$. The interaction of the unsteady wake and the turbulent separation bubble is characterized by the normalized wake passing frequency, St_H, and the Reynolds number, Re_H. These two dominant parameters are defined as

$$\text{St}_H = f_p H / U_\infty, \tag{1}$$

$$\text{Re}_H = U_\infty H / \nu, \tag{2}$$

where U_∞ is the free-stream velocity and f_p is the wake passing frequency determined by the rotational speed of the cylindrical rods and the number of rods. A free-stream velocity of $U_\infty = 6.0\,\text{m/s}$ was used in the present experiments, resulting in a Reynolds number of $\text{Re}_H = 5600$. The experimental conditions used in the present work were the same as in Chun and Sung (2003).

Synchronized measurements of wall-pressure and velocity were made using a joint experimental set-up integrating a 16-channel microphone array (Soritel Inc.) and a hotwire anemometry system (TSI IFA100/300) with a split film probe (TSI 1288). The 16 ICP-type microphones used to detect the wall-pressure fluctuations were installed on the perforated surface of the blunt body. The split-film probe was used to survey the u and v velocity components of the flow field in the mid-span plane. Simultaneous signals of the wall pressure and velocity were acquired using an A/D board (DT2839). Details regarding the instrumentation can be found in Chun and Sung (2003).

3. Maximal overlap discrete wavelet transform

To resolve the spatial and temporal interaction between the unsteady wakes and the scale-variant flow structures buried in the turbulent separation bubble, the MODWT was adopted for the MRA of the wall-pressure fluctuations and velocity fluctuations in the separation bubble. Prior to showing the resultant data, it should be mentioned that the fundamentals of the MODWT are well summarized in Percival and Walden (2000).

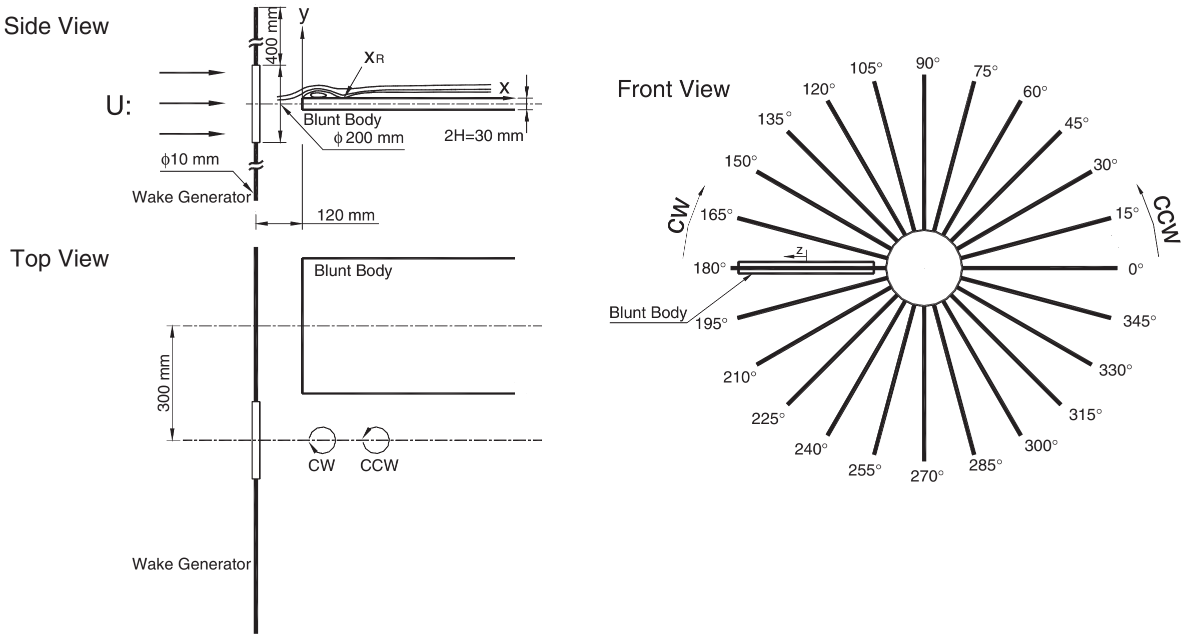

Fig. 1. Blunt body with wake generator.

Although the MODWT has the same computational load as the fast Fourier transform (FFT), it has better potential for scale-variant analysis of instantaneous signals. This is of prime significance in detecting intermittent behavior of a turbulent separated flow. By using the MODWT, a temporal signal X can be extracted to a series of MRA signals, e.g., band-passed details D_n, $D_{n-1}, \ldots$, D_2, D_1 at successively smaller central frequency levels, as well as a low-passed smooth S_n:

$$X = \sum_{j=1}^{n} D_j + S_n. \tag{3}$$

The details D_j and the smooth S_n are defined by the inverse transform of a pyramid algorithm associated by zero-phase filters (Percival and Walden, 2000). This means that the MRA signals of simultaneously measured data at different spatial positions are kept in phase, yielding a wealth of information on unsteady turbulent flow events.

In the present study, the MRA outlined above was applied to the wall-pressure and velocity fluctuations, which were simultaneously measured using the microphone array and the hot-wire anemometer, respectively. Thus, both the wall-pressure and velocity fluctuations were decomposed into D_j and S_n. In order to clearly disclose unsteady events such as large-scale vortex shedding, the MRA component of the wall-pressure fluctuations at D_j was employed as a conditional signal to synchronize the MRA component of the velocity fluctuations at D_j. The same procedure was applied to the S_n to yield the potential low-frequency motion.

An instructive example of the MRA conducted using the MODWT is illustrated in Fig. 2. A time-series of wall-pressure signals is resolved to D_1–D_7 and S_7, the central frequencies of which are determined by the sampling frequency of the wall-pressure signal and shown in Table 1. The signal denoted by ‘Pressure’ in Fig. 2 is the measured wall-pressure signal. The horizontal axis denotes an arbitrary time scale. At D_1, the smallest scale of the wall-pressure fluctuations is shown at 300, 400 and 500 along the time axis, while the larger scale of the wall-pressure appears at times 30, 230, and 390 in D_2. Instantaneous patterns similar to that in D_2 are produced at the lower frequencies D_3 and D_4. Inspection of the curves at D_5–D_7 discloses the periodic motions of large-scale vortices. S_7 denotes the rest of the analyzed signals, which constitutes the slowest motion of the wall-pressure fluctuations. The shapes of D_1–D_7 and S_7 in the frequency domain displayed in Fig. 2 reveal the logarithmic relationship between the neighboring scales as provided by turbulent cascade theory when they are displayed in the frequency domain through the Fourier transform (Pope, 2000). The curve at $\mathrm{St}_{D1} = 4.12$ indicates the highest fluctuation frequency, which reflects the influence of the smallest eddies on the wall-pressure. In this frequency range, the measured wall-pressure must be almost random due to turbulent fluctuations. The shapes of the curves in the frequency domain at D_2–D_7 are similar. The most energetic large-scale vortices are buried in D_7, as determined from the previous observation that the vortex shedding frequency is $\mathrm{St} = 0.09$ for this system (Chun and Sung, 2002). S_7 contains the major components of the flapping frequency at $\mathrm{St} = 0.02$. Note that the original signal ‘pressure’ is restored by superposing all the D_j and S_n.

4. Results and discussion

Unsteady events such as the shedding of large-scale vortical structures and the flapping motion of a separation bubble are inherent features of the separated and reattaching turbulent flows that occur over a blunt body (Kiya and Sasaki, 1983, 1985). These unsteady events are significantly impacted by the introduction of an unsteady wake in the incoming flow. Chun and Sung (2002) systematically studied the separated and reattaching flow under the influence of unsteady wakes with variable frequencies and rotation directions. Compared with the reattachment length of the separated flow of $x_R = 7.0$ obtained at $\mathrm{St}_H = 0$, the reattachment lengths in the presence of a CW or CCW rotating unsteady wake were optimally reduced to $x_R = 4.0$ and 2.4, respectively, for $\mathrm{St}_H = 0.2$. Given that knowledge of the instantaneous scale-variant flow structures would place us in a better position to understand the complex unsteady behaviors in the turbulent shear flow, we simultaneously measured the wall-pressure fluctuations and the velocity fluctuations using a microphone array and a split-film anemometer. This enabled us to delineate the intermittent unsteady events superimposed in the turbulent shear flow by using MRA. On the basis of the findings of Chun and Sung (2002) outlined above, we focused our attention on the intermittent interaction between the unsteady wakes and the scale-variant flow structures at $\mathrm{St}_H = 0$ and 0.2 (CW, CCW).

Prior to directly examining the unsteady patterns of flow structures, we calculated the auto-correlation of the continuous wavelet transformed wall-pressure to see the footprints of the vortical structures (Chun et al., 2004; Liu et al., 2005). Based on the Mexican hat wavelet, the CWT of a real-time series of data is defined as

$$wf(b,a) = \frac{1}{a}\int_{-\infty}^{\infty} f(t)\Psi\left(\frac{t-b}{a}\right)\mathrm{d}t, \tag{4}$$

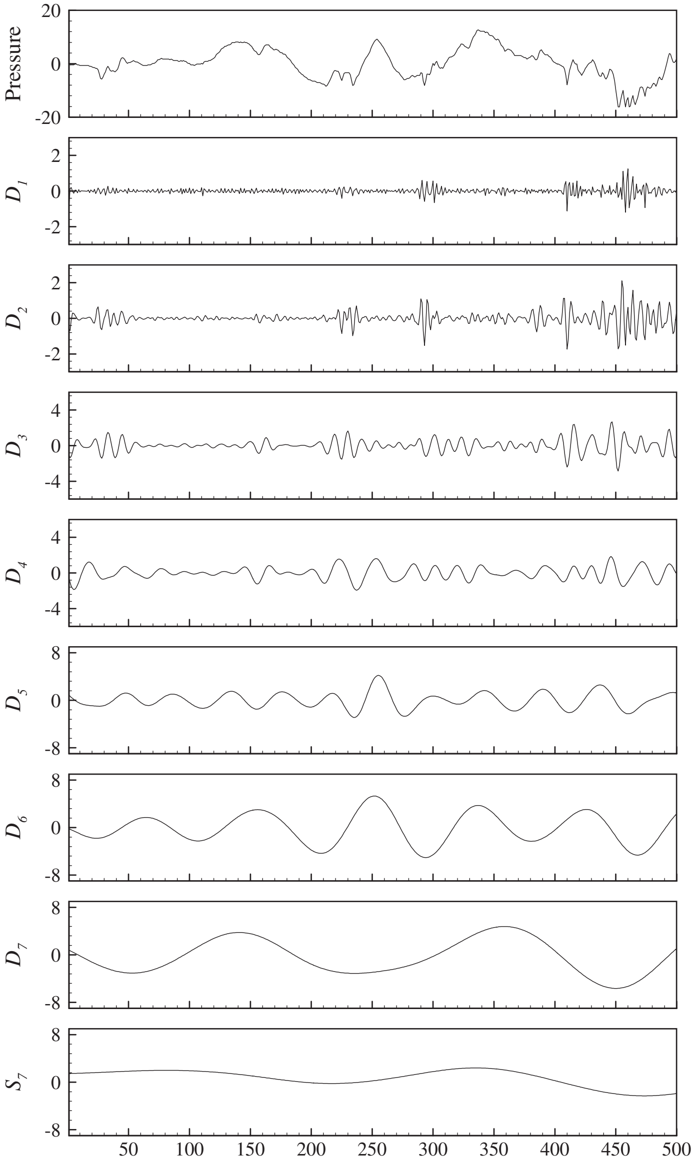

Fig. 2. Multi-resolution analysis in the time domain by MODWT. The frequencies corresponding to D_1–D_7 and S_7 are shown in Table 1.

Table 1
Nondimensional center frequency of wavelet filters

	D_1	D_2	D_3	D_4	D_5	D_6	D_7	S_7
St	4.12	2.14	1.06	0.53	0.26	0.13	0.08	0.03

where a is the time-scale dilation parameter, b is the time transition parameter, and Ψ is the Mexican hat wavelet, $\Psi(t) = (1 - t^2)\exp(-0.5t^2)$. The wavelet auto-correlation function is given as

$$wc(a,\tau) = \lim_{T\to\infty} \frac{1}{T}\int_{-T/2}^{T/2} wf(b,a)\,wf(b+\tau,a)\,\mathrm{d}b, \tag{5}$$

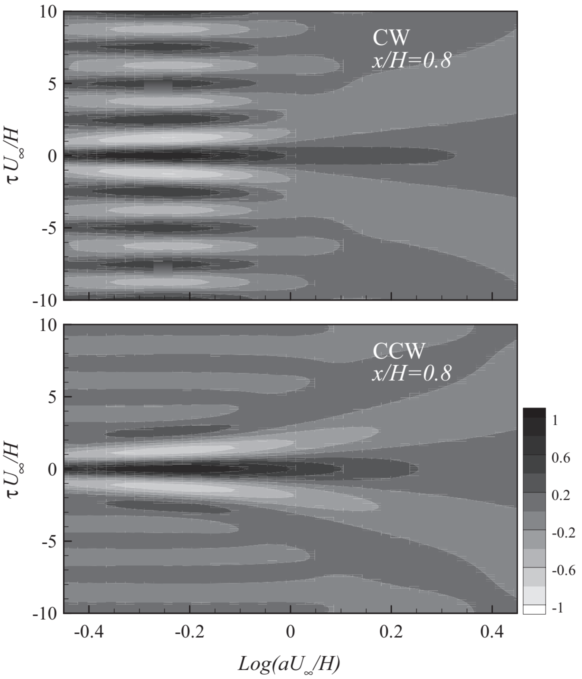

Fig. 3. Auto-correlation of continuous wavelet transformed wall-pressure at $x/H = 0.8$.

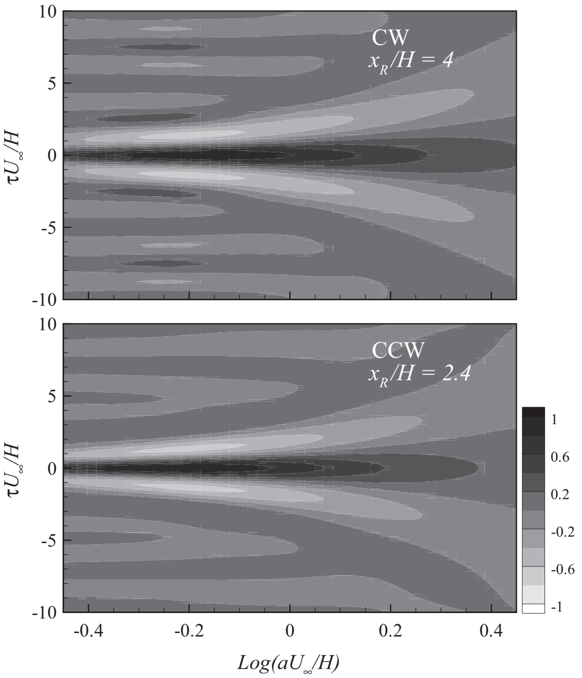

Fig. 4. Auto-correlation of continuous wavelet transformed wall-pressure at $x_R/H = 2.4$ and 4.0.

where τ is the time delay of wavelet coefficients in the wavelet space. The auto-correlation of the continuous wavelet transformed wall-pressure at $x/H = 0.8$ (i.e., immediately downstream of the separation edge) is displayed in Fig. 3. Periodic signatures of the unsteady wakes are subsequently generated with 1 period in $2.5\tau U_\infty/H$ at

$\log(aU_\infty/H) = -0.25$ ($\mathrm{St} = 0.2$) for both CW and CCW conditions. When the wake generator rotation is CW, the unsteady wakes are very strong; under CCW rotation, by contrast, the wakes are significantly attenuated, suggesting that there should be enhanced mixing between the unsteady wakes and the vortical structures in the separation bubble. Inspection of the auto-correlation along $\tau U_\infty/H = 0$ reveals a large-amplitude correlation region extending down to low frequency and two other discrete areas near $\log(aU_\infty/H) \simeq 0$ ($\mathrm{St} = 0.09$) at $\tau U_\infty/H = \pm 2$. In the CCW rotation, the low-frequency region is not fully separated from the footprints of the unsteady wakes, indicating stronger interaction between the unsteady wakes and the large-scale vortical structures than is observed in the CW rotation. Fig. 4 displays the auto-correlation of the CWT of the wall-pressure at the reattachment point, i.e., $x_R/H = 4$, for CW rotation and at $x_R/H = 2.4$ for CCW rotation. For both cases, the discernible wake signatures are much weaker than those in the CW rotation. However, comparison of the time interval along $\tau U_\infty/H$ discloses that the unsteady wakes in the system with CCW rotation decay faster than those in the CW rotation system. This difference is due to differences in the approaching velocity component of the unsteady wakes to the blunt body, which give rise to different flow regimes, described previously as ‘cutting’ and ‘wrapping’ regimes (Chun and Sung, 2002).

We now turn to the instantaneous patterns of the vortical structures and the influence of unsteady wakes on those structures. The continuous wavelet coefficients of the velocity components at $\mathrm{St} = 0.2$ were deduced using the CWT and then conditionally averaged using the wall-pressure as a conditional signal. The intermittent variation of conditionally averaged wavelet coefficients is a manifestation of the fluctuating velocity strength induced by the large-scale vortical structures. Hence, the continuous wavelet coefficients of the streamwise and the wall-normal velocity components were

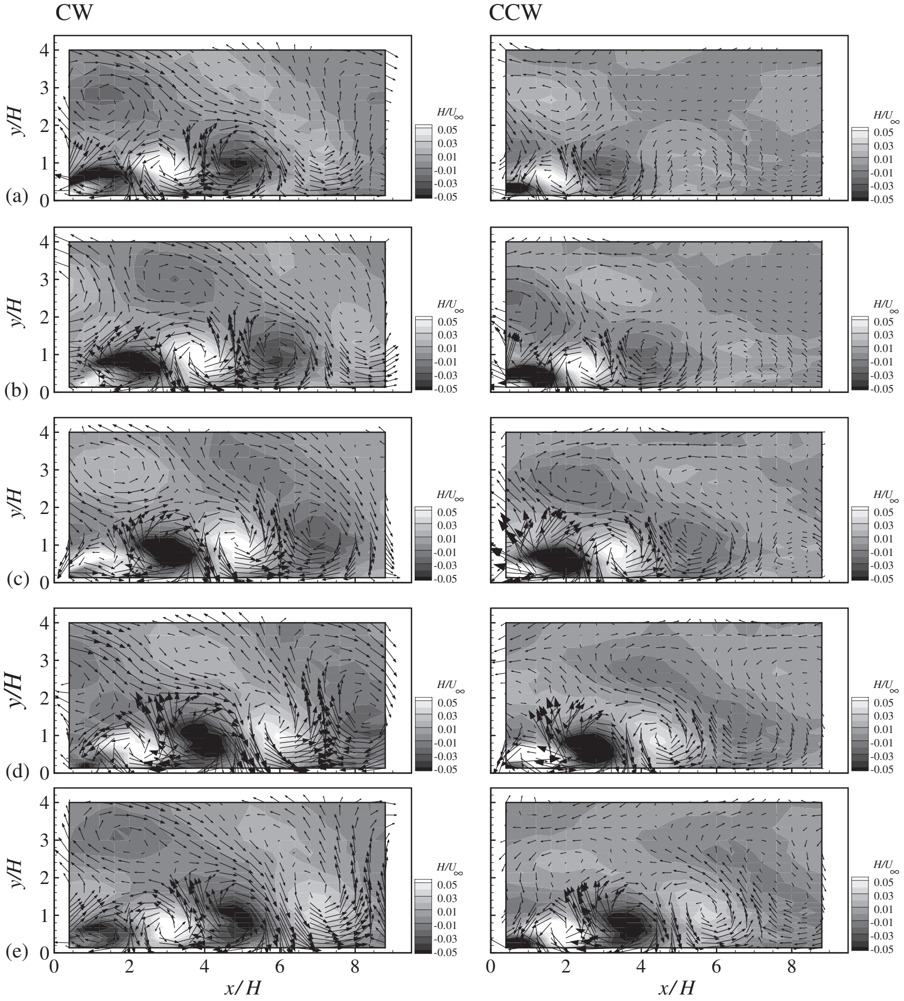

Fig. 5. Conditional averaging of continuous wavelet coefficients at $\mathrm{St}_H = 0.2$: (a) $\tau = -T/2$, (b) $\tau = -T/4$, (c) $\tau = 0$, (d) $\tau = T/4$, (e) $\tau = T/2$, where T is the period of wake oscillation.

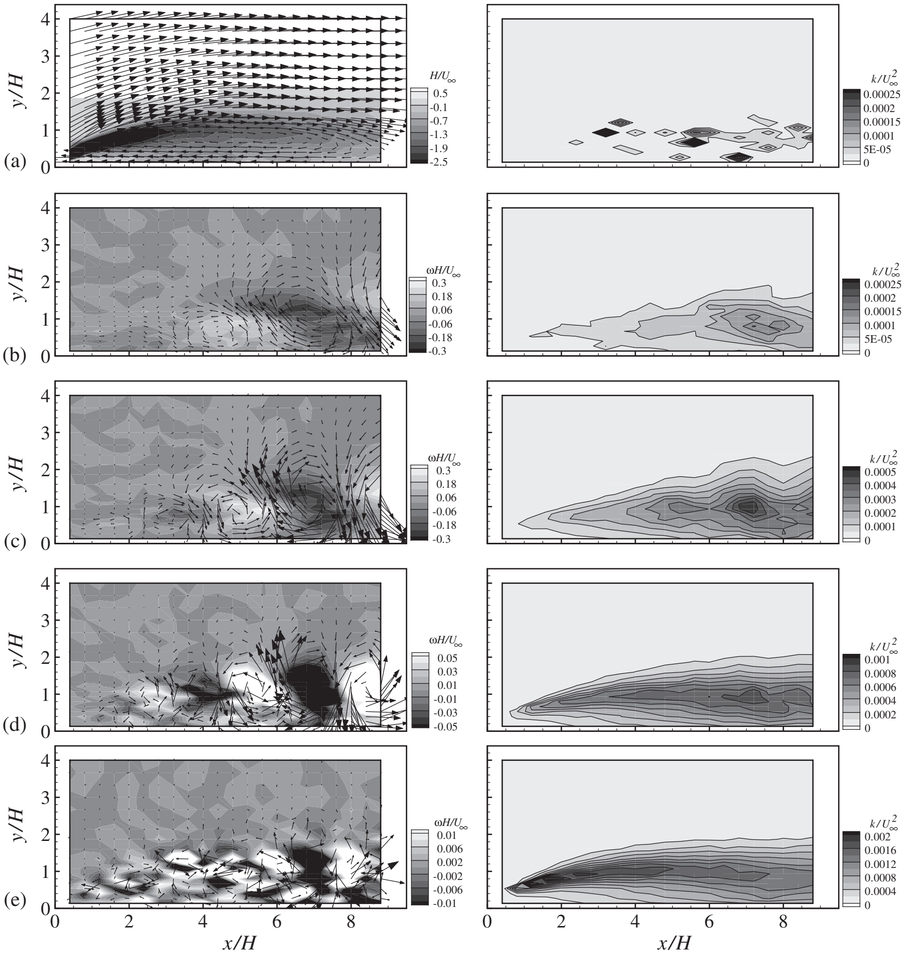

Fig. 6. Multi-resolution analysis in velocity field at $\mathrm{St}_H = 0$: (a) St = 0.03, (b) St = 0.08, (c) St = 0.13, (d) St = 0.26, (e) St = 0.53.

vectorized and plotted in Fig. 5. In addition, contour plots of the instantaneous spanwise vorticity were generated to better understand the vortical structures. Under both the CW and CCW rotation conditions, upper and lower vortical structures are observed in the turbulent separated flow. The upper structure is related to the unsteady wake in the free-stream and the lower structure is superimposed in the turbulent separation bubble. The upper structure is followed by the lower co-rotated structure. The presence of two coherent structures can be explained in terms of the 'cutting' or 'wrapping' regimes of the flow (Chun and Sung, 2002). In the CCW rotation, the size of the lower structure becomes smaller than that in the CW rotation, although no clear difference is observed in the size of the unsteady wake in the upper structure. This indicates that the enhanced mixing with the coherent structure that occurs when the rotation direction of the wake generator is changed from CCW to CW has only a limited effect inside the separation bubble.

Fig. 6 shows the MRA velocity field at $\mathrm{St}_H = 0$. Recall that the amplitudes of the velocity signals are dramatically reduced by increasing the filtering frequency; thus the length of the displayed vectors has an arbitrary unit for visualization purposes. At St = 0.03, the conditionally averaged velocity field shows a recirculation region in the turbulent separation bubble. The recirculation region is stationary in $0 \leqslant x/H \leqslant 9$, being the averaged flow structure of the turbulent separation bubble. The spanwise vorticity is concentrated in the initial phase of flow separation along the shear layer in $0 \leqslant x/H \leqslant 2$, and the turbulent kinetic energy is almost zero. At St = 0.08, some counter-rotating flow structures are observed (Fig. 6(b)). Forming downstream of $x/H = 4$, the structure at St = 0.08 is inclined toward the upstream direction, resulting in an elliptical shape. The location of the maximum turbulent kinetic energy, $(x/H, y/H) = (7.2, 1)$, coincides with the center of the vortical structure due to the existence of a large-scale vortex in the turbulent separation bubble (Kiya and Sasaki, 1985). However, no maximum in the turbulent kinetic energy was found in the counter-rotating structures. At St = 0.13, a smaller flow structure is detected (Fig. 6(c)). Maxima in the turbulent

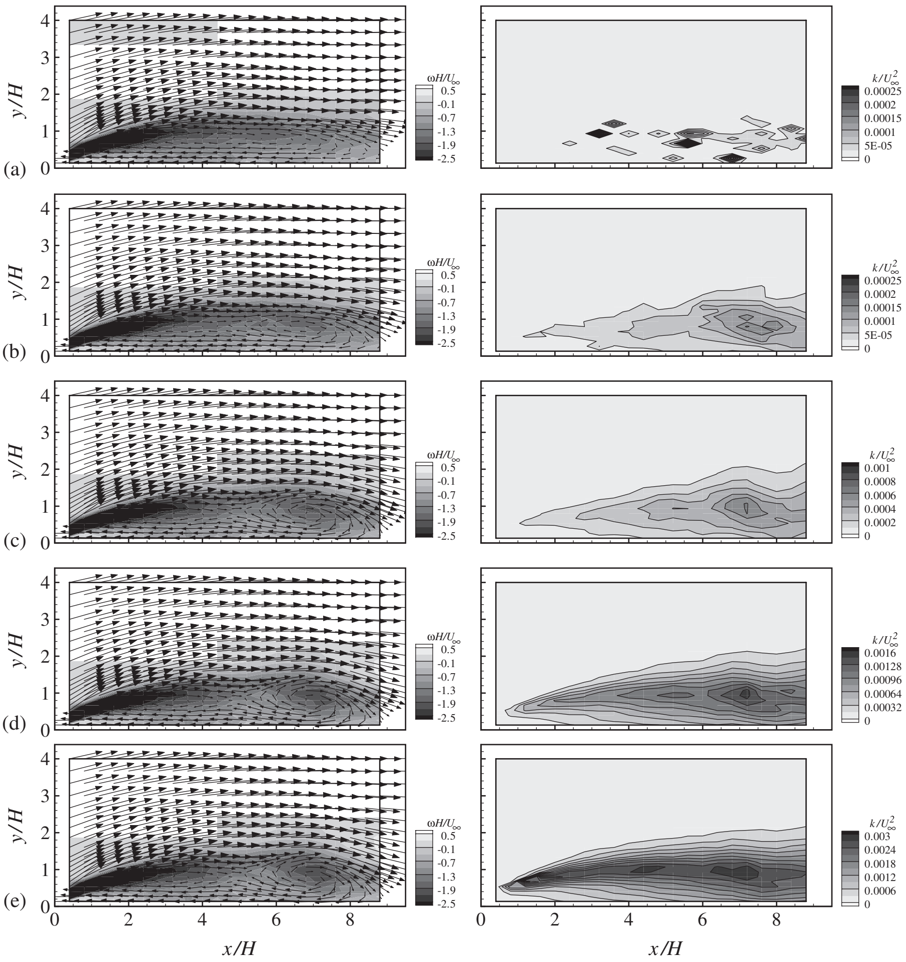

Fig. 7. Superposition of resolved velocity field at $\mathrm{St}_H = 0$: (a) $\mathrm{St} = 0.03$, (b) $\mathrm{St} < 0.08$, (c) $\mathrm{St} < 0.13$, (d) $\mathrm{St} < 0.26$, (e) $\mathrm{St} < 0.53$.

kinetic energy are located at $(x/H,\ y/H) = (7.2,\ 1)$ and $(5.2,\ 1)$. When the frequency is increased to $\mathrm{St} = 0.26$, the amplitudes of the spanwise vorticity and velocity fluctuations are reduced (Fig. 6(d)). At this frequency, the flow structures are well-organized and trace further upstream, and the turbulent kinetic energy is still increasing without convergence. Close inspection of Fig. 6(d) reveals that the turbulent kinetic energy is concentrated in the shear layer edge of the turbulent separation bubble. At $\mathrm{St} = 0.53$ (Fig. 6(e)), the velocity distribution and spanwise vorticity show a high degree of randomness; this randomness is attributed to the limitation of the spatial resolution of the measurement stations. Thus, the spatial resolution of $\Delta x/H = 0.8$ was insufficient to resolve flow structures at frequencies greater than $\mathrm{St} = 0.26$. It is noteworthy that the turbulent kinetic energy of small-scale vortices is concentrated in the area immediately downstream of the separation edge.

In an effort to see the contribution of unsteady events associated with different frequencies to the flow pattern, we reconstructed the scale-variant velocity field by successively adding higher scales (Fig. 7). By superposing $\mathrm{St} = 0.08$ onto the averaged recirculation region of the separated bubble at $\mathrm{St} = 0.03$, an elliptical shape appears at $(x/H,\ y/H) = (7.2,\ 1)$. Combined with the distribution of turbulent kinetic energy, the elliptical shape is regarded as a turbulent structure. The recirculation region and the large-scale vortical structure are located in $0 \leqslant x/H \leqslant 5$ and $5 \leqslant x/H \leqslant 9$, respectively. Superposition of the flow velocity at $\mathrm{St} = 0.13$ clarifies the saddle point at $(x/H,\ y/H) = (4.8,\ 0.8)$, and imposition of $\mathrm{St} = 0.26$ enhances the formation of large-scale vortical structure. By including $\mathrm{St} = 0.53$, the turbulent kinetic energy shown in Fig. 7(e) is concentrated on the initial phase of flow separation along the shear layer edge. The velocity fields at $\mathrm{St} = 0.26$ and 0.53 make smaller contributions to the conditionally averaged vortical structure than the velocity fields at $\mathrm{St} = 0.08$ and 0.13. However, the velocity at higher frequency has a stronger influence on the turbulent kinetic energy distribution. Note that the locations of maximum turbulent kinetic energy are $(x/H,\ y/H) = (1.4,\ 0.6)$,

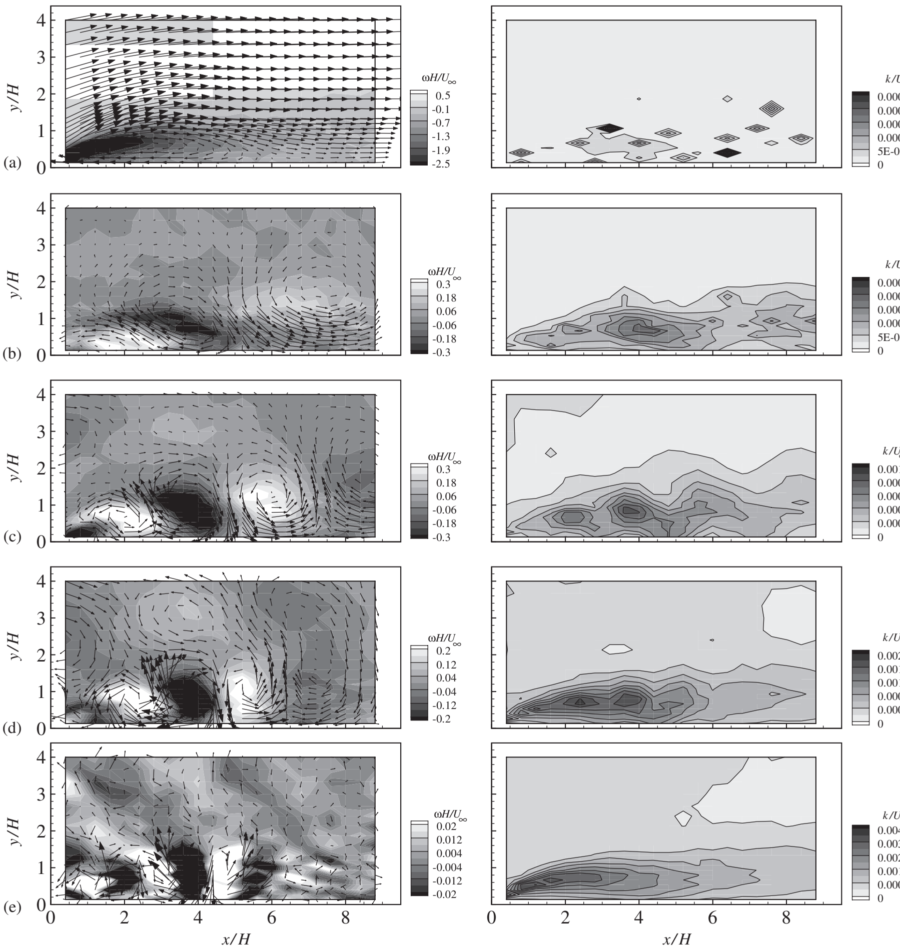

Fig. 8. Multi-resolution analysis in velocity field at $\mathrm{St}_H = 0.2$ and CW: (a) St = 0.03, (b) St = 0.08, (c) St = 0.13, (d) St = 0.2, (e) St = 0.53.

(4.4, 0.8) and (6.4, 0.8) in Fig. 7e. The saddle point and the local maximum of turbulent kinetic energy coincide at $(x/H, y/H) = (4.4, 0.8)$, a manifestation of the engulfment of the turbulent flow into the separation bubble. The other two locations of maximum turbulent kinetic energy agree well with the results of Kiya and Sasaki (1983, 1985).

The influence of the unsteady wakes passing from the wake generator with CW rotation on the scale-variant flow field is seen in Fig. 8. Similar to the flow structure at $\mathrm{St}_H = 0$, the distribution of flow velocity at St = 0.03 yields a stationary recirculation region in $0 \leqslant x/H \leqslant 5.6$. At St = 0.08, a flow structure with large circulation at $(x/H, y/H) = (7.2, 2)$ is observed (Fig. 8(b)), which can be attributed to the unsteady wake impingement on the turbulent separation bubble. The flow structure at $(x/H, y/H) = (4, 0.7)$ coincides with the location of maximum turbulent kinetic energy, indicating that it is the large-scale vortex (Kiya and Sasaki, 1985). At St = 0.13 and 0.26, the upper and lower flow structures are prominent. The upper vortical structure at $y/H \leqslant 1.5$ is due to the unsteady wakes, and the effect of these wakes is more visible at St = 0.26 than at 0.13. The lower vortical structure results from the interaction between the unsteady wakes and the blunt body according to the ‘cutting’ regime (Chun and Sung, 2002). The lower flow structure is clearer at St = 0.13, because the shedding frequency is lower than the wake passing frequency (Chun and Sung, 2002). Regular formation of vortical structures is observed at St = 0.13 and 0.26. Maxima of the turbulent kinetic energy are observed at $(x/H, y/H) = (2.2, 0.6)$ and (3.8, 0.8). According to the criterion proposed by Kiya and Sasaki (1985), the absence of a turbulent kinetic energy maximum in the upper region indicates that the upper vortical structure is not a turbulent vortex. At St = 0.26 (Fig. 8(d)), the two separated flow structures begin to merge, because the turbulent shear layer has little influence on the unsteady wakes after the reattachment at $x_R/H = 4$. This mixing between turbulent and nonturbulent flow structures leads to a reduction in the turbulent kinetic energy. The conditionally averaged velocity

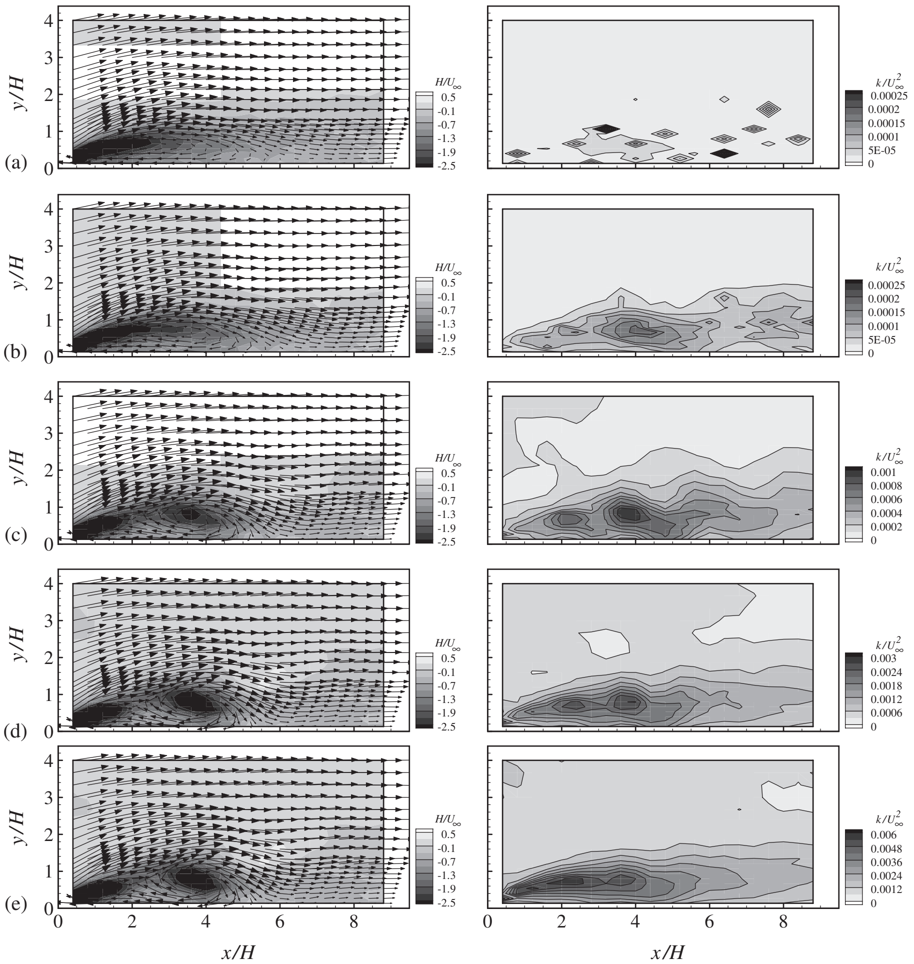

Fig. 9. Superposition of resolved velocity field at $\mathrm{St}_H = 0.2$ and CW: (a) $\mathrm{St} = 0.03$, (b) $\mathrm{St} < 0.08$, (c) $\mathrm{St} < 0.13$, (d) $\mathrm{St} < 0.26$, (e) $\mathrm{St} < 0.53$.

field at $\mathrm{St} = 0.53$ shows organized coherent structures in the separation bubble. Compared with $\mathrm{St}_H = 0$, the large-amplitude turbulent kinetic energy is limited to the initial phase of flow separation along the shear layer.

To resolve the influence of vortices at successively increasing frequencies on the flow field, which is disturbed by the CW rotation of the wake generator, we reconstructed the flow field by serially adding higher frequency signals (Fig. 9). At $\mathrm{St} = 0.03$, a recirculation region is observed in $0 \leqslant x/H \leqslant 5.6$. Superposition of $\mathrm{St} = 0.08$ divides the recirculation region into two parts: the recirculation region confined within $0 \leqslant x/H \leqslant 2$ and a large flow structure within $2 \leqslant x/H \leqslant 5.6$. The center of the flow structure coincides with the location of maximum turbulent kinetic energy, indicating the presence of a turbulent vortex. Another maximum of the turbulent kinetic energy is found at $(x/H, y/H) = (2.4, 0.7)$, possibly reflecting turbulent engulfment between two consecutive vortices. The location of the turbulent kinetic energy maximum at $(x/H, y/H) = (2.4, 0.7)$ also indicates that the small-scale turbulent motions reside in the separation bubble when the large-scale vortex sheds from the recirculation region. As shown in Fig. 8(e), the concentration of the turbulent kinetic energy along the initial phase of the separated shear layer is primarily due to contributions from the shedding vortices centered at $\mathrm{St} = 0.53$.

The influence of the CCW rotating wake generator on the flow field is revealed by the scale-variant flow field shown in Fig. 10. At $\mathrm{St} = 0.03$, the size of the recirculation region in $0 \leqslant x/H \leqslant 3.6$ is reduced by the unsteady wakes. At $\mathrm{St} = 0.08$, a large-scale flow structure is observed at $(x/H, y/H) = (5.6, 1.6)$ due to the unsteady wakes. However, the flow structure at $x/H = 2.0$ consists of two parts, at $y/H = 0.5$ and 1.5, where the deformation of the latter part is due to the 'wrapping' regime of the flow (Chun and Sung, 2002). The lower part is a turbulent vortical structure that is elongated by the interaction of the unsteady wakes and the blunt body. The coherent structure at $\mathrm{St} = 0.13$ is divided

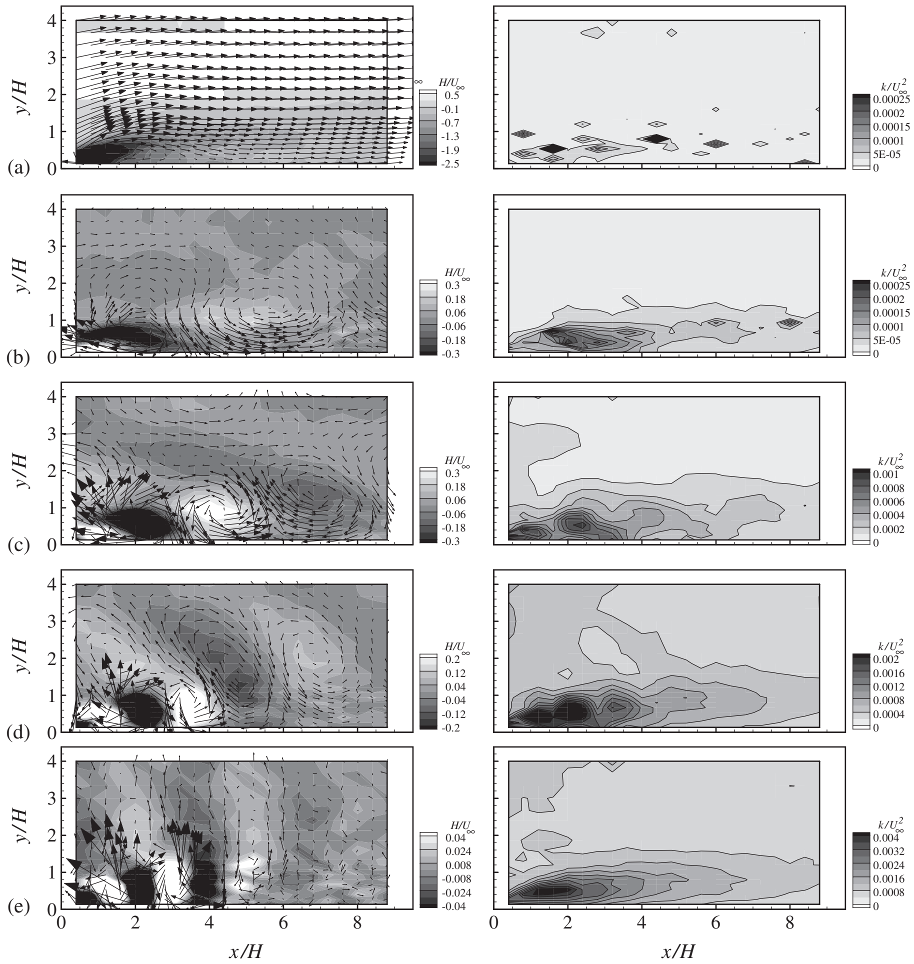

Fig. 10. Multi-resolution analysis in velocity field at $\mathrm{St}_H = 0.2$ and CCW: (a) St = 0.03, (b) St = 0.08, (c) St = 0.13, (d) St = 0.26, (e) St = 0.53.

into three parts (Fig. 10(c)). The buffer region between the two flow structures within $2 \leqslant y/H \leqslant 3$ is due to the effect of the 'wrapping' process. Examination of the turbulent kinetic energy maxima at $(x/H, y/H) = (0.8, 0.4)$ and (2.4, 0.6) reveals that the flow structure moves toward the blunt body by $0.2\,H$. At St = 0.26, coalescence of the lower and upper flow structures takes place $2\,H$ earlier in the streamwise direction than was observed in the system with CW rotation. The flow structure at St = 0.53 is well-organized, with the development of the spanwise vorticity in the wall-normal direction.

The reconstruction of the multi-scale resolved flow velocity for the case of CCW rotation is shown in Fig. 11. A recirculation region is observed in $0 \leqslant x/H \leqslant 2.8$ at St = 0.03. Superposition of the flow at St = 0.08 divides the recirculation region into two parts: $0 \leqslant x/H \leqslant 1.2$ and $1.2 \leqslant x/H \leqslant 2.8$. At St = 0.13, the maximum turbulent kinetic energy is observed at $(x/H, y/H) = (2.2, 0.6)$, in good agreement with the position of the turbulent vortical structure. Another turbulent kinetic energy maximum is observed at $(x/H, y/H) = (1.2, 0.4)$, which is a saddle point located between the recirculation region and the large-scale turbulent vortex. No clear difference in the mean flow field with increasing frequency is observed in Fig. 11, indicating that the small-scale flow structure makes only a small contribution to the time-averaged flow pattern, although it induces the large-scale velocity fluctuations. The intensification of turbulent kinetic energy with increasing frequency level observed in Figs. 11(a)–(e) demonstrates that the large-scale velocity fluctuations are induced from the small-scale vortices.

To verify the effect of superposition at different center frequencies, space-time contour plots of the conditionally averaged streamwise velocity at $y/H = 0.13$ are shown in Figs. 12–14. The space–time contours are used to investigate

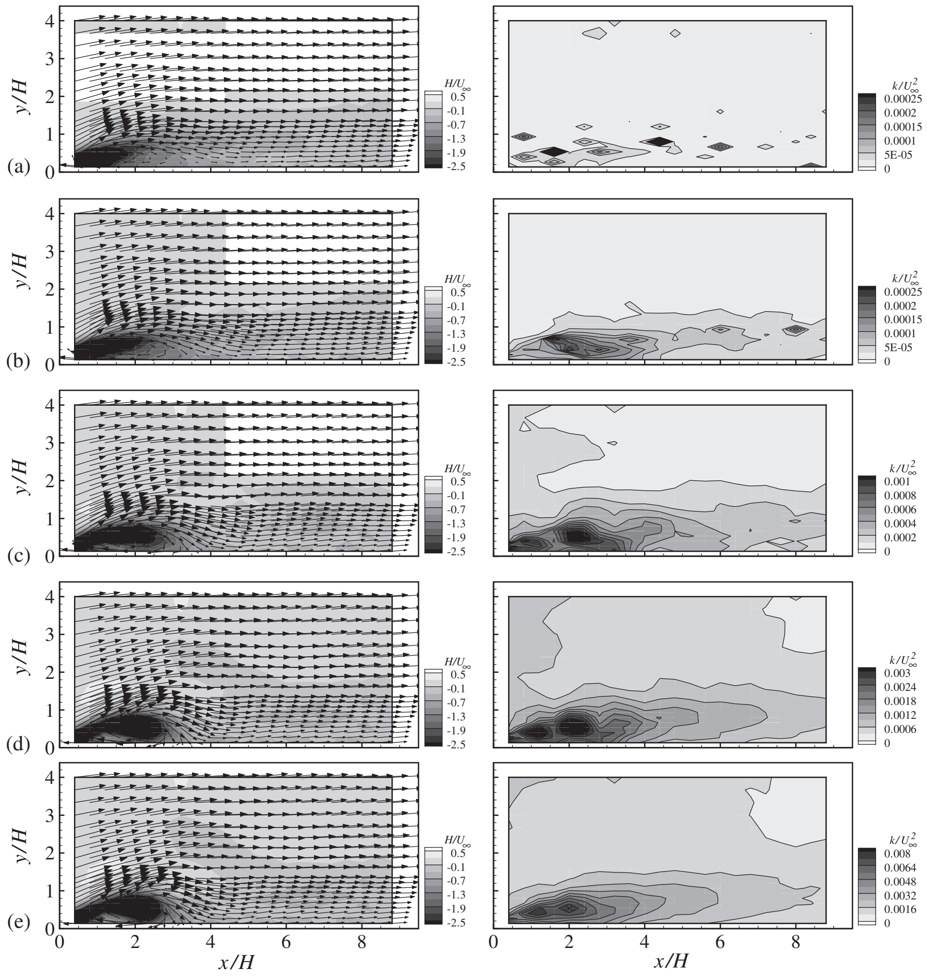

Fig. 11. Superposition of resolved velocity field at $\mathrm{St}_H = 0.2$ and CCW: (a) $\mathrm{St} = 0.03$, (b) $\mathrm{St} < 0.08$, (c) $\mathrm{St} < 0.13$, (d) $\mathrm{St} < 0.26$, (e) $\mathrm{St} < 0.53$.

the sawtooth movement of the separation bubble (Kiya and Sasaki, 1985; Lee and Sung, 2002; Chun and Sung, 2003). In Fig. 12, a reattachment point is located at the contour of $u/U_\infty = 0$, which is almost fixed in the streamwise coordinate. The reduction in reattachment length when CW or CCW rotation conditions are applied can be seen by comparing the plots at $\mathrm{St} = 0.03$ (Figs. 12(b) and (c)) with the $\mathrm{St}_H = 0$ data (Fig. 12(a)). No clear unsteadiness of the reattaching region is seen at this low frequency, consistent with previous results showing that this system undergoes a flapping motion at $\mathrm{St} = 0.03$ (Chun and Sung, 2002).

On increasing the frequency to $\mathrm{St} = 0.08$, shrinkage and enlargement of the separation bubble occur with a range of motion of $1H$. The recirculation region is represented as a dead zone, while the reattaching region indicates much more complex motions in which the size of the reattachment length increases and decreases. When the frequency is further increased to $\mathrm{St} = 0.13$, the shrinkage and enlargement motions become clear (Fig. 14). At $tU_\infty/H = -3$, the separation bubble is divided into three parts and there are more than two reattachment points. In the presence of the unsteady wakes, the reattaching flow is found to undergo periodic upstream movements whose period is set by the phase of the shrinkage and the enlargement of the separation bubble. This movement is called the sawtooth movement of the separation bubble (Kiya and Sasaki, 1985), and originates from the large-scale vortex shedding. Although this phenomenon becomes clearer as the frequency increases, most of the essential features are observed in the range $\mathrm{St} < 0.13$. Considering the reported vortex shedding frequency at $\mathrm{St} = 0.09$ by Chun and Sung (2002), this means that the sawtooth movement is more strongly related to the vortex shedding than to the flapping motions (Kiya and Sasaki, 1985; Kiya et al., 1997). The flapping motions are observed at the contour line of $u/U_\infty = 0.2$ for $\mathrm{St}_H = 0$ and at $u/$

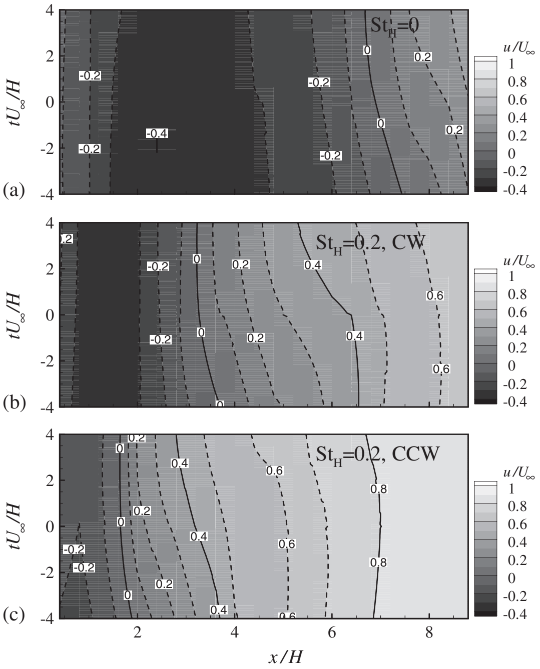

Fig. 12. Streamwise velocity contour at $y/H = 0.13$ and St $= 0.03$.

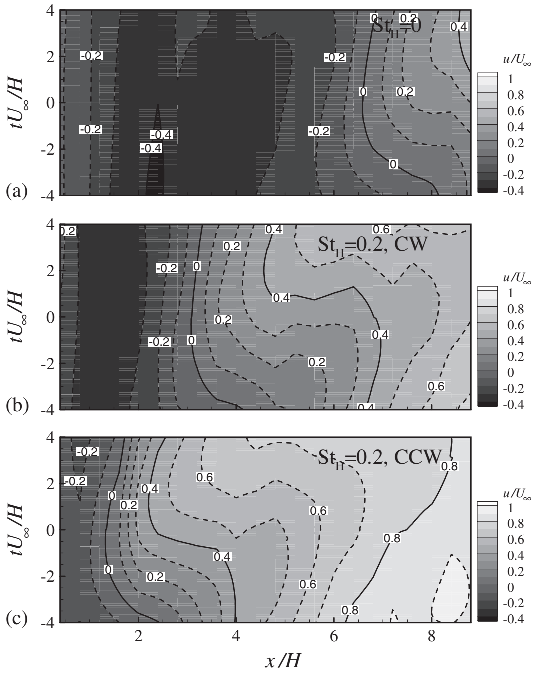

Fig. 13. Streamwise velocity contour at $y/H = 0.13$ and St$<$0.08.

$U_\infty = 0.4$ for the systems with CW or CCW rotation, as shown in Fig. 12. The period of this movement is greater than $tU_\infty/H = 8$ and the range of movement is less than $0.4\,H$. The amplitude of the flapping motions is so small that they are rarely noticed due to the presence of the sawtooth movement, as shown in Figs. 12–14.

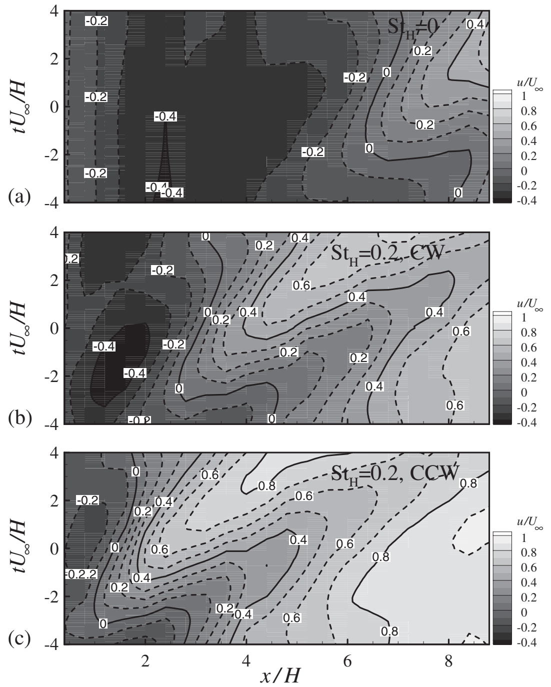

Fig. 14. Streamwise velocity contour at $y/H = 0.13$ and $\mathrm{St} < 0.13$.

5. Conclusions

In the present work, multi-resolution analysis (MRA) based on the maximal overlap discrete wavelet transform (MODWT) was extensively employed to delineate the unsteady events buried in a turbulent separation bubble disturbed by unsteady wakes. Particular attention was directed toward the intermittent interaction between the unsteady wakes and the scale-variant vortical structures at $\mathrm{St}_H = 0$ and 0.2 (CW, CCW). To study this interaction, we simultaneously measured the wall-pressure fluctuations and velocity fluctuations using a microphone array and a split-film anemometer, respectively. Conditional averaging was applied to capture the unsteady events associated with the shedding of large-scale vortical structures. Preliminary analysis based on the continuous wavelet transform (CWT) demonstrated that the unsteady wakes in the CCW configuration mixed well with the large-scale vortical structures buried in the separation bubble, which resulted in faster decay than was observed in the CW configuration. Using MRA, we found that most of the energy content in coherent structures was concentrated in the large-scale vortices and the initial phase of flow separation. Addition of three velocity fields from the lowest scale (i.e., $\mathrm{St} = 0.03$, 0.08 and 0.13) was sufficient to reconstruct a converged time-averaged coherent structure. Spatial and temporal plots of the streamwise velocity verified the presence of flapping motions as well as the sawtooth movements of reattachment points, which were reported in a previous study on the same system.

References

Chun, S., Sung, H.J., 2002. Influence of unsteady wake on a turbulent separation bubble. Experiments in Fluids 32, 269–279.

Chun, S., Sung, H.J., 2003. Large-scale vortical structure of a turbulent separation bubble affected by unsteady wake. Experiments in Fluids 34, 572–584.

Chun, S., Liu, Y.Z., Sung, H.J., 2004. Wall-pressure fluctuations of turbulent separated and reattaching flow affected by unsteady wake. Experiments in Fluids 37, 531–546.

Funazaki, K., 1996a. Unsteady boundary layers on a flat plate disturbed by periodic wakes: part I—measurement of wake-affected heat transfer and wake-induced transition model. ASME Journal of Turbomachinery 118, 327–336.

Funazaki, K., 1996b. Unsteady boundary layers on a flat plate disturbed by periodic wakes: part II—measurements of unsteady boundary layers and discussion. ASME Journal of Turbomachinery 118, 337–346.

Han, J.C., Zhang, L., Ou, S., 1993. Influence of unsteady wake on heat transfer coefficient from a gas turbine blade. Journal of Heat Transfer 115, 904–911.

Kiya, M., Sasaki, K., 1983. Structure of a turbulent separation bubble. Journal of Fluid Mechanics 137, 83–113.

Kiya, M., Sasaki, K., 1985. Structure of large-scale vortices and unsteady reverse flow in the reattaching zone of a turbulent separation bubble. Journal of Fluid Mechanics 154, 463–491.

Kiya, M., Shimizu, M., Mochizuki, O., 1997. Sinusoidal forcing of a turbulent separation bubble. Journal of Fluid Mechanics 342, 119–139.

Lee, I., Sung, H.J., 2002. Multiple-arrayed pressure measurement toward the investigation of the unsteady flow structure of a reattaching shear layer over a backward-facing step. Journal of Fluid Mechanics 463, 377–402.

Li, H., 2002. Application of wavelet multi-resolution analysis to pressure fluctuations of gas-solid two-phase flow in a horizontal pipe. Powder Technology 125, 61–73.

Liu, X., Rodi, W., 1992. Measurements of unsteady flow and heat transfer in a linear turbine cascade. ASME Paper No. 92-GT-323.

Liu, X., Rodi, W., 1994. Surface pressure and heat transfer measurements in a turbine cascade with unsteady oncoming wakes. Experiments in Fluids 17, 171–178.

Liu, Y.Z., Kang, W., Sung, H.J., 2005. Assessment of the organization of a turbulent separated and reattaching flow by measuring wall pressure fluctuations. Experiments in Fluids 38, 485–493.

Minniti III, R.J., Mueller, T.J., 1998. Experimental investigation of unsteady aerodynamics and aeroacoustics of a thin airfoil. AIAA Journal 36, 1149–1156.

Percival, D.B., Walden, A.T., 2000. Wavelet methods for time series analysis. Cambridge University Press, Cambridge.

Pope, S.B., 2000. Turbulent Flows. Cambridge University Press, Cambridge.